Deformation heterogeneity in cellular Al alloys revealed by surface deformation analysis

A. -F. Bastawros
Division of Engineering and Applied Sciences, Harvard University, Cambridge, MA 02138
A. G. Evans
Materials Institute, Princeton University, Princeton, NJ 08540, USA

Abstract

The mechanisms of compressive deformation that occur in both closed and open cell Al alloys have been established using digital image correlation analysis. Closed cell materials exhibit three stages of deformation. The first involves localized plastic straining at nodes. It occurs uniformly and leads to a nominal loading modulus appreciably lower than the stiffness. The second comprises discrete bands of concentrated strain containing membranes that experience plastic buckling, elastically constrained by surrounding cells. In this phase, previously formed bands harden, giving rise to new bands that form in neighboring regions. The localized bands exhibit a long-range correlation separated by 3-4 cells. This length scale characterizes the continuum limit. Thirdly, coincident with a stress peak, one of the bands exhibits complete plastic collapse. As the strain increases, this process repeats, subject to small stress oscillations around the peak stress. Open cell materials exhibit more homogeneous deformation up to the onset of global yielding. Localized deformation bands coincide with the peak stress. They exhibit a similar modulus upon loading and unloading and follow the predictions of regular cellular solids.

1 Introduction

The mechanical performance of cellular metals governs their utility in various applications, such as cores for ultralight sandwich panels/shells, as well as crash or blast absorbing systems [1-2]. From an application perspective, the most important properties are the elastic stiffness, the yield strength and the "plateau" stress at which the material compresses plastically. Macroscopically, the strength and stiffness of open cell foams were shown [1-2] to follow theoretical predictions of regular solids [1]. Conversely, closed cell foams yield at a relative strength appreciably lower than theoretically realizable for *regular* cellular solids (periodic structure with no defects) [1-2]. Knockdown factors of 3 to 10 are typical [3], because of morphological defects. Experimental assessments of these and other defects are sparse. Preliminary observations have suggested that the dominant degrading features include cell ellipticity and non-planar membranes [3-5]. Theoretical studies affirm the importance of curves and wiggles in the membranes that governs the elastic stiffness and limit load [5-6].

The plastic response of cellular metals has been visualized by surface deformation measurements, using digital image correlation [7-8], as well as by X-ray computed tomography [4]. Open cell foam (Duocel®, $\rho \approx 0.08$, $\sigma_0 \approx 1.5\text{MPa}$, $E \approx 0.5GPa$) exhibited

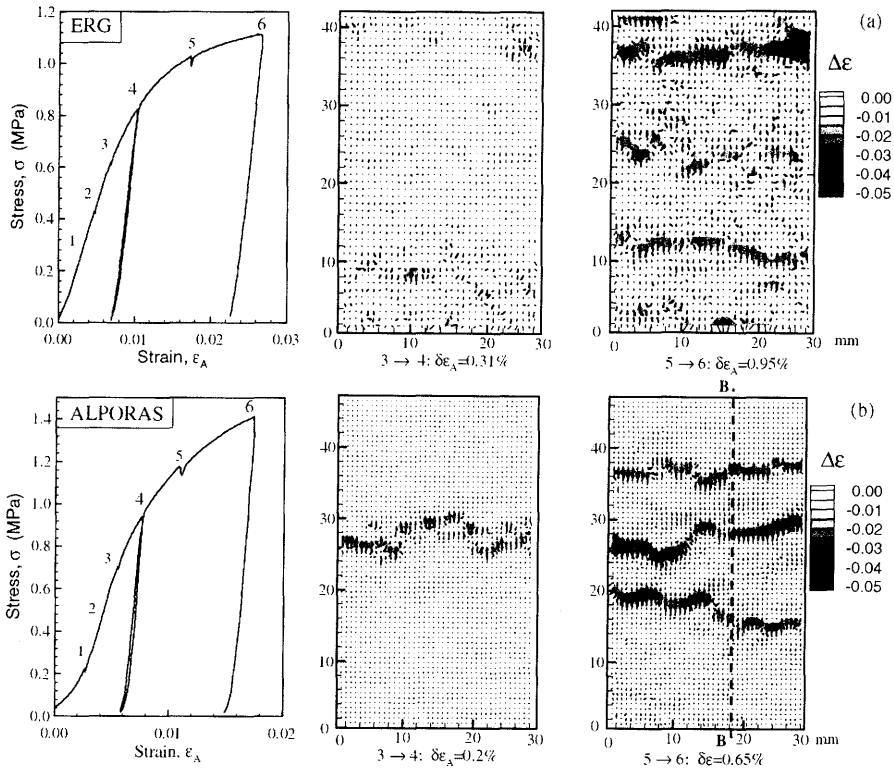

Fig. 1: Surface strain maps of the incremental distortion strain, $\Delta\varepsilon$.

homogeneous deformation up to the onset of global yielding (Fig. 1a). Localized deformation bands coincide with the peak stress. Conversely, the deformation of closed cell foam (ALPORAS® [9], $\rho \approx 0.07$, $\sigma_o \approx 1.3MPa$, $E \approx 0.7-1.0GPa$) [3,10] is manifest as bands containing cells that collapse plastically (Fig. 1b). These bands establish the onset of yielding, the hardening and the level of the plateau stress (Fig. 2a). Multiple bands form as deformation continues, until the gauge section attains a densified state.

This paper summarizes the mechanisms operating at the cell/membrane level in closed cell foam by following the evolution of the deformation with cell-level resolution. It is achieved by devising a digital image correlation procedure [7-8] and using commercial Surface Displacement Analysis (SDA) Software [11]. Details of the analysis are found elsewhere; [8,12,13]. The displacement field is used to evaluate the Eulerian (Almansi) strain tensor and the spin tensor over the current configuration [14]. The cell distortions were characterized using the difference between the maximum and the minimum principal strains, $\Delta\varepsilon \equiv |\varepsilon_{11} - \varepsilon_{22}|$ (see Fig. 1). The combination of the distortion with the rotation around the third axis, ω_z, provides information about cell deformation mechanisms. These results are used to assess the limit of the continuum mean-field constitutive framework and to establish the characteristic length scale that governs the non-local response.

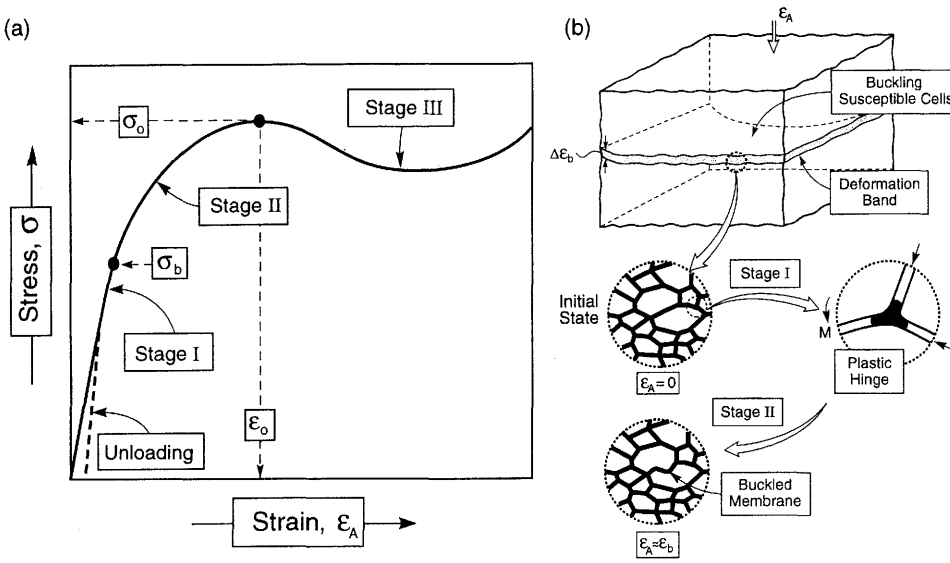

Fig. 2: A schematic indicating the phenomena that occur during the three stages of plastic deformation in a closed cell Al alloy foam subjected to compression.

2 Mechanical response

2.1 Macroscopic response

The early stress/strain response ($\varepsilon_A < 0.05$) of closed cell foam exhibits three stages (Fig. 2a). *Stage I,* at macroscopic axial strains, $\varepsilon_A < \varepsilon_b$, wherein the deformation is nominally linear, but the tangent modulus is lower than the unloading modulus. *Stage II,* at $\varepsilon_b \leq \varepsilon_A \leq \varepsilon_o$, characterized by macroscopic non-linearity, yet subject to appreciable strain hardening, with a tangent modulus that decreases rapidly with increase in strain and reaches zero at ε_o. *Stage III,* at $\varepsilon_A \geq \varepsilon_o$, which commences with a stress maximum at ε_o, followed by a region of strain softening, with subsequent stress oscillations about a gradual overall strain hardening.

2. 2 Cell level deformation

The closed cell foam deformation histories for incremental loading, followed by unloading, are presented in Fig. 1b. The superimposed vectors represent the magnitude and direction of the maximum principal strain. These *incremental* distortion maps reveal that localized deformation bands having width about one-cell diameter initiate at the onset of nonlinearity. Each band sweeps the entire specimen cross section. Within each band, there are cell-sized regions that exhibit strain levels about an order of magnitude larger than the applied strain. Outside the bands, the average strains are small and within the elastic range. The principal strains reveal that the flow vectors are primarily in the loading direction, normal to the band plane, indicative of a crushing mode of deformation. Moreover, the incremental distortion maps show new sets of collapse bands that form in regions neighboring previously formed bands. Further details of band evolution are given in [15].

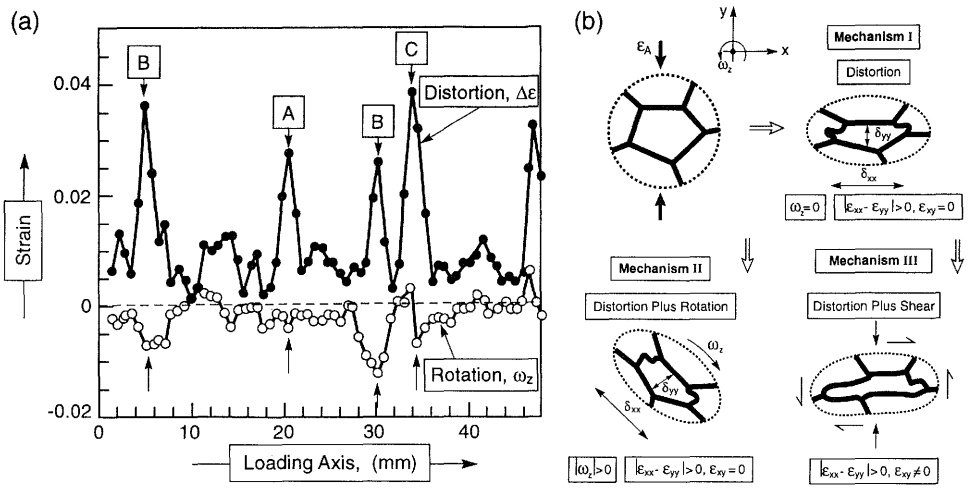

Fig. 3: (a) Distortional and rotational strains as a function of the axial position (line B-B on Fig.1b) with the corresponding deformation mode indicated. (b) Mechanisms attributed to these strains. Mechanism I refers to band A, mechanism II to band B and mechanism III to band C.

The strain maps (Fig. 1b) are suggestive of a periodicity in the deformation bands. That is, the bands appear to attain a characteristic spacing along the loading direction as stage III is approached. This effect is more comprehensively revealed upon testing the larger specimens [15]. Now, as $\varepsilon_A \rightarrow \varepsilon_o$, the cross section contains many bands, that develop a spacing of 3-4 cell diameters.

The combination of distortional and rotational deformations found at various sites along the axis (Fig. 3) suggests at least three possible mechanisms at the cell-level. Mechanism (I) represents sites subject to large distortions but zero rotation. This happens at site (A) on Fig. 3a, with the cell distortions indicated. Mechanism (II) at site (B) involves the same distortion, but now combined with a clockwise rotation, as indicated by the sketch. For this rotation to be accommodated, neighboring cells must rotate counterclockwise. Mechanism (III), at site (C), combines distortion with in-plane shear. At this site, within the region occupied by the distortional strain peak, the rotation has symmetric positive and negative peaks about the localized band center. This feature signifies an in-plane shear deformation having the characteristics illustrated on the sketch.

3 Deformation Mechanisms

The preceding observations and measurements show that surface observed cell distortions (Figs. 1,3) are similar and follow the deformation characteristics of the fully constrained bulk cells as revealed by X-ray imaging [4,15]. They collectively provide some understanding of the deformation mechanisms in each of the three stages identified on Fig. 2.

In *Stage I*, there is no evidence of either strain concentrations (from mapping) or cell distortions (from X-ray images). Yet, the slope of the loading curve is appreciably lower than the unloading modulus. Local plastic deformations occurring at cell nodes is implied, as previously ascertained from numerical calculations [5]. Cell face wiggles as well as residual

stresses may also deteriorate the initial stiffness by inducing localized membrane plasticity. The response envisaged is sketched on Fig. 2b, wherein the moment on the membrane at the left causes a plastic hinge. In this sketch, the effect of membrane stresses is considered to be insignificant, because of stress relaxation induced by defects (cell face cracks and wiggles). This very important phenomenon results in a "soft" initial loading modulus, which degrades the performance of this material as a core for sandwich panels/shells. Further analysis is needed to identify cell structures that minimize plastic activity at small strains, below ε_o.

In *Stage II*, cell distortions arise at multiple cells along a band of material one cell diameter in width. The distortions involve phenomena based on geometric and material nonlinearities: (i) plastic buckling manifest as a snap-through of cell membranes followed by localized membrane plasticity; (ii) bending of at least one membrane in each of the susceptible cells. Despite these inelastic mechanisms, the cells do not collapse. Those cells most susceptible to distortion are relatively elliptic "*non-equi-axed*" and contain curved or wiggled membranes. The plastic buckling and bending of individual membranes induces strain concentrations in neighboring cells and causes both elastic distortion and rotations (Fig. 3). If the neighboring cells have comparable strength, the resulting stress redistribution will be sufficient to localize deformation in an entire layer of cells, normal to the loading axis. However, these strains must be *insufficient* to cause a buckling instability in contiguous cells along the loading axis, perhaps because an elastic enclave is retained (Fig. 2a). This enclave would provide a hardening mechanism that deactivates the band. This is why deformation occurs in discrete bands, rather than throughout the entire gauge region. Along the loading axis, each band has an accommodation domain, several cell layers in width. This accommodation establishes a length scale, which sets limits on the material volume amenable to analysis by continuum methods. This finding suggests that the band kinematics are governed by the level of accommodation around each defect rather than the local defect state. Accordingly, there may be effects of specimen length on band formation. These issues, as well as a detailed model, await further studies.

In *Stage III*, one of the bands that formed in stage II experiences complete plastic collapse. The strain concentrations in cells adjacent to those that experienced earlier plastic buckling and bending must now attain levels required for buckling. This process is autocatalytic and instantaneously spreads the collapse across the entire loaded section, probably because of the transfer of the stored energy into the collapse band from the elastically loaded section of the gauge length. The collapsed band does not propagate normal to its plane. Instead, it stiffens its environs, causing the collapse process to repeat in different regions of the gauge area, each time coinciding with a macroscopic stress oscillation. There are also residual strains originating either at locally induced bands (as at smaller strains), or from regions in contact with the platens.

4 Concluding remarks

The measurements and observations of cell-level distortions and rotations accompanying the formation of deformation bands have established some factors that govern the inelastic response of commercial, closed cell metal foams. Morphologically defective cells result in bands of enhanced deformation. Within each band several constituent membranes experience plastic buckling and bending, but others remain elastic. This interaction happens despite the spatial randomness of the defective cells. The membrane buckling/bending results in cell distortions accommodated by rotation and in-plane shear. The band kinematics enforce their

evolution with a characteristic spacing of about 4 cells. This length scale governs the material volume below which continuum models cannot be applied.

Upon continued straining, one of the bands develops a high distortion rate. This band collapses, plastically, resulting in a stress peak, σ_o and progressive softening. The deformation kinematics lock the collapse band and allow subsequent hardening. Thereafter, other bands collapse, subject to an oscillating stress around σ_o, with moderate strain hardening.

While this study has identified some key elements of the deformation response, they do not provide a straightforward means for analysis and simulation. Nevertheless, they highlight the complexity of the non-local effect as well as the interaction length scale. To address these factors, a model that combines stochastic aspects of defective cells with a mechanics of membrane deformation and their interactions appears to be needed, comparable to that for the tensile failure of composites [16,17].

Acknowledgements

This work is supported by the DARPA/ONR through MURI grant No. N00014-1-96-1028 on the Ultralight Metal Structure project at Harvard University.

References

[1] L. J. Gibson, M. Ashby, *Cellular Solids*, Cambridge University Press, New York (1997)

[2] A. G. Evans, J. W. Hutchinson, M. Ashby, Prog. Material Science, in press (1998)

[3] Y. Sugimura, J. Meyer, M. Y. He, H. Bart-Smith, J. Grenestedt, A. G. Evans, Acta Mater. 45, 5245 (1997)

[4] H. Bart-Smith, A. -F. Bastawros, D. R. Mumm, A. G. Evans, D. Sypeck, H. G. Wadley, Acta Mater. 46, 3583 (1998)

[5] A. E. Simone, L. J. Gibson, Acta Mater. 46, 3929 (1998)

[6] J. Grenestedt, J. Mech. Phys. Solids 46, 29 (1998)

[7] A. -F. Bastawros, R. McManuis, R., Exp. Tech. 22, 35 (1998)

[8] A. -F. Bastawros Exp. Mech., *to be submitted* (1999)

[9] S. Akiyama, H. Ueno, K. Imagawa, A. Kitahara, S. Nagata, K. Morimoto, T. Nishikawa, M. Itoh, U. S. Patent 4, 713, 277 (1987)

[10] A. E. Simone, L. J. Gibson, Acta Mater. 46, 3109 (1998)

[11] Instron, Surface Displacement Analysis User Manual (1997)

[12] E. O. Brigham, *The Fast Fourier Transform*, Prentice-Hall, Inc., New Jersey (1974)

[13] D. J. Chen, F. P. Chiang, Y. S. Tan, H. S. Don, Applied Optics 32, 1839 (1993)

[14] L. E. Malvern, *Introduction to the Mechanics of a Continuous Medium*, Prentice-Hall, New Jersy (1969)

[15] A. -F. Bastawros, H. Bart-Smith, A. G. Evans, J. Mech. Phys. Solids, *in press* (1999)

[16] W. A. Curtin, Phys Rev. Lett. 80, 1445 (1998)

[17] M. Ibnabdeljalil, W. A. Curtin, Int. J. Solids Struct. 34, 2649 (1997)